Journal of the Mechanics and Physics of Solids 124 (2019) 411–426

Contents lists available at ScienceDirect

Journal of the Mechanics and Physics of Solids

journal homepage: www.elsevier.com/locate/jmps

Rigidity of hemispherical elastic gridshells under point load indentation

Changyeob Baek[a], Pedro M. Reis[b,*]

[a] Department of Mechanical Engineering, Massachusetts Institute of Technology, Cambridge, MA 02139, USA
[b] Flexible Structures Laboratory, Institute of Mechanical Engineering, École Polytechnique Fédérale de Lausanne, Lausanne, CH-1015, Switzerland

ARTICLE INFO

Article history:
Received 16 July 2018
Revised 19 October 2018
Accepted 7 November 2018
Available online 8 November 2018

Keywords:
Rigidity
Gridshell
Chebyshev net

ABSTRACT

We present results from physical and numerical experiments on the rigidity of hemispherical gridshells under point load indentation. By systematically exploring the relevant parameters of the system, we provide a scaling law for the rigidity of elastic gridshells in terms of the dimension of the structure and the number of rods it contains, as well as the geometric and material properties of the individual rods. Our approach combines a set of precision desktop-scale experiments and discrete elastic rod simulations, which are found to be in excellent quantitative agreement. Our proposed empirical relation for the rigidity also points to the underlying nonlocal nature of the mechanical response of gridshells, in contrast to the local response of isotropic continuum shells. We further assess this nonlocality by quantifying the resulting radial displacement field as well as inspecting the effect of the location of the indentation point on the rigidity.

1. Introduction

Elastic gridshells comprise regular planar grids of thin elastic rods, which, by the loading of their extremities along a predetermined path, can be actuated into three-dimensional shell-like structures. Having first appeared in architecture in the 1970s, the design of this class of structure was initially informed primarily by rudimentary empirical guidelines obtained from prototypes with networks of suspended chains (Hennicke et al., 1974; Liddell, 2015). Subsequently, the emergence of computer-aided design in architecture has revolutionized the rational design of gridshells, thereby alleviating the cumbersome procedures of building physical prototypes and allowing for a more systematic exploration of the parameter space. Since then, substantial research has been focusing on the computational form-finding of gridshells (Bulenda and Knippers, 2001; Hernández et al., 2013; Lefevre et al., 2015), with several successful cases realized in practice (Baverel et al., 2012; Hennicke et al., 1974; Quinn and Gengnagel, 2014).

Beyond the realm of architecture, the idea of using buckling and the ensuing elastic deformation of an originally two-dimensional (2D) structural layout to generate three-dimensional (3D) structures has also emerged in other branches of engineering and in the physical sciences. The idea of recognizing and exploiting mechanical instabilities for function (shaping, in this particular case), instead of the more traditional engineering mechanics perspective of regarding them as the onset of structural failure, is at the heart of the burgeoning '*Extreme Mechanics*' community (Reis et al., 2015; Reis, 2015).

* Corresponding author.
E-mail address: pedro.reis@epfl.ch (P.M. Reis).

https://doi.org/10.1016/j.jmps.2018.11.002
0022-5096/

Consequently, there has been an upsurge in geometry-driven structures that aligns well with this '*from failure to function*' paradigm shift. Within this framework, one can inverse-engineer the shapes of this class of structures by strategically harnessing the underlying geometry and the subsequent large deformations that occur past the onset of instability. Examples of geometry-driven structures, to name just a few, include origami (Dudte et al., 2016; Miura, 1985; Overvelde et al., 2017; Tachi, 2013), kirigami (Castle et al., 2014; Shyu et al., 2015; Zhang et al., 2015), microfabrication of complex structures through the buckling of ribbons adhered to a pre-stretched substrate (Fu et al., 2018; Xu et al., 2015), and growth-induced morphogenesis (Erb et al., 2013; Gladman et al., 2016; van Rees et al., 2017; Savin et al., 2011).

In previous work of our own, we interpreted the geometry-driven actuation process of gridshells by adopting the theory of smooth Chebyshev nets (Baek et al., 2018). In this framework, the inverse-design of gridshell is done by sampling the continuous domain of the Chebyshev net of the specific target surface. As an example, we showed that the known Chebyshev solution for a hemisphere yields nearly hemispherical gridshell (more details on Section 2), even if the physical structure also includes a series of mechanical ingredients (*e.g.*, the mechanical properties of the underlying rods and the joints between them) that are not considered in Chebyshev's geometric description. This approach also renders us a tool to quantitatively describe the kinematics of the actuated gridshells by translating the notion of Gaussian curvature into the quadrangular regions on the gridshell enclosed by the rods. Furthermore, our past work highlighted the importance of nonlocality in this class of systems, which we demonstrated by considering their response to point loading. However, since the theory of Chebyshev nets is purely geometric, our attention focused entirely on kinematics. In the current study, we turn to the mechanics of gridshell structures by quantifying their rigidity (force per unit indentation displacement) under point-load indentation.

Since the seminal theoretical studies on the rigidity of isotropic continuum double-curvature shells (Pogorelov, 1988; Reissner, 1946), numerous physical experiments and simulations are performed (Lazarus et al., 2012; Nasto et al., 2013; Nasto and Reis, 2014; Vaziri and Mahadevan, 2008; Vella et al., 2012), to successfully connect the three pillars: theory, experiments, and simulations. More specifically, Vaziri and Mahadevan (2008) identified two distinct types of the response of the shells – local and nonlocal deformation – depending on the geometry of the surface. In particular, for positively curved shells, the deformation is localized around the indentation, suggesting that structural properties are also local to the indentation. Indeed, Lazarus et al. (2012) and Vella et al. (2012) had shown that the rigidity of a positively curved shell depends only on its local geometry.

However, the connection between the geometry and mechanics, including the importance of nonlocality, remains poorly understood for gridshells. There have been attempts to rationalize the mechanics of nets using Chebyshev's kinematics (Pipkin, 1984; Rivlin, 1955; Wang and Pipkin, 1986; 1987). This approach has been adopted for the analysis of textiles with well-defined families of fibers (Tschebyscheff, 1878; Van West et al., 1990). More recently, several authors have investigated variants of Chebyshev nets. For example, Steigmann (2018) considered a Chebyshev net with finite in-plane torsional stiffness between two families of fibers. In another recent study, Poincloux et al. (2018) considered the mechanics of knits, which can be viewed as a special type of Chebyshev net that allow slippage between the fibers and their points of contact. However, these past studies only addressed relatively simple planar geometries and there is still a considerable gap in understanding the mechanics of more complex networked structures. As such, there are opportunities to develop predictive descriptions for the mechanical properties of complex-shaped gridshells, which can be readily used as a predictive framework for their design.

Here, as a first step to understand the mechanics of doubly-curved elastic network structures, we perform a quantitative study of the rigidity of hemispherical gridshells. First, we make use of data from physical and computational experiments to obtain an empirical reduced description, in the form of a scaling law, for the rigidity of hemispherical gridshells at their pole, as a function of the various physical parameters. We find that all the rods in the structure contribute to its rigidity, thereby highlighting the nonlocality of gridshells rooted in the underlying hyperbolic Gauss equation. We then devise two sets of numerical experiments that further manifest this nonlocality: the interpolated displacement map under point-load indentation with the varying number of rods constituting the gridshells, and the rigidity away from the pole. In the first set of experiments, we seek to directly quantify the nonlocal displacement field, finding that it has an asymptotic convergence as the number of rods increases. The second set of simulations yields a nontrivial and non-monotonic increase of the rigidity for indentation points away from the pole; again, a reflection of nonlocality. Overall, the rich behavior that we observe in hemispherical gridshells calls motivates the need for theoretical developments, which we hope our work will instigate.

Our manuscript is structured as follows. In Section 2, we define the problem that we set out to investigate and introduce our model system, which is based in our previous work (Baek et al., 2018). We also briefly present the theory of Chebyshev nets. In Section 3, we delineate the procedure to obtain nearly hemispherical gridshells and report the measurements of their rigidity obtained through desktop-scale experiments and computer simulations. In Sections 4 and 5, we systematically study the dependence of the rigidity of hemispherical gridshells on the relevant geometric and physical parameters. An empirical scaling law is proposed that successfully collapses all of the data into three master curves, depending on the number of rods in the structure. As an aside, we look into the gridshell composed of a single set of orthogonal rods and rationalize its rigidity using the theory of Euler's elastica. In Section 6, we investigate the spatial heterogeneity of the displacement field caused by the indentation. Finally, Section 7 is dedicated to the physical and numerical experiments on the sensitivity of the rigidity on the location of indentation. Section 8 summarizes our findings and identifies directions of possible future research.

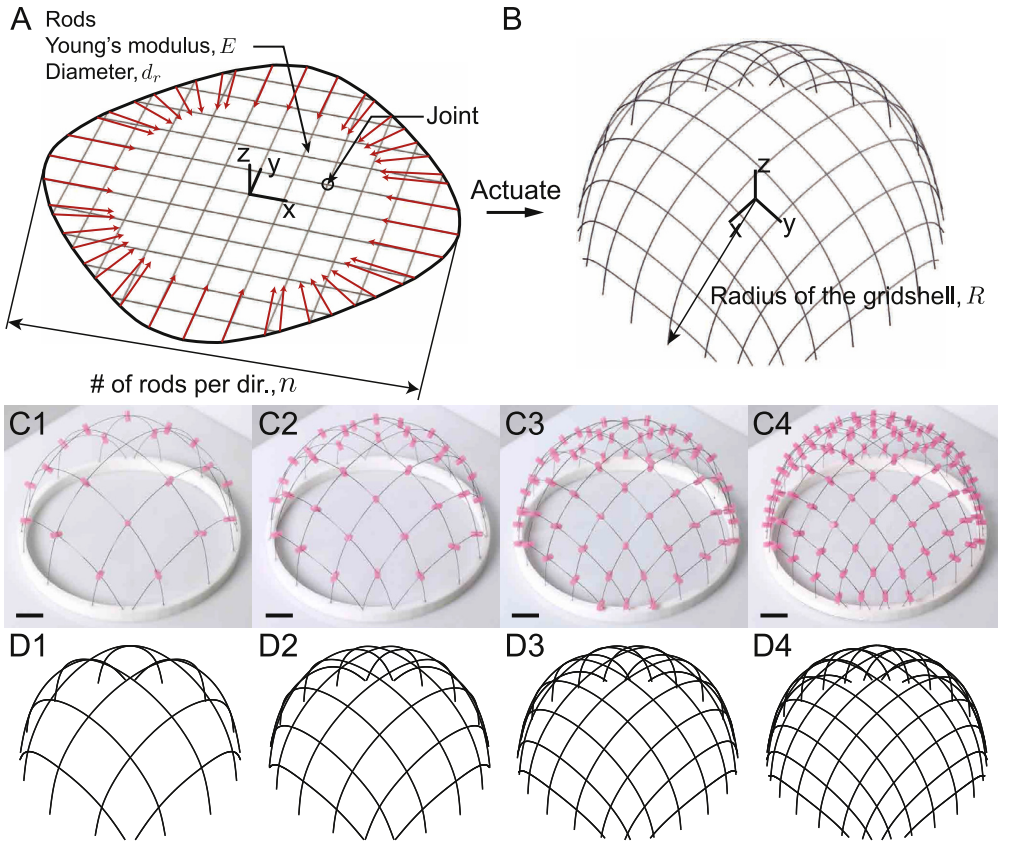

Fig. 1. (A) A grid for the hemispherical gridshell, with $n = 11$, $d_r = 0.254$ mm, and $R = 61.1$ mm. Black solid line is the boundary for the hemispherical Chebyshev net confining the grid inside the boundary (rendered image). Actuating the extremities of the grid along the actuation path (red arrows) yields a gridshell. (B) Rendered image of the resulting hemispherical gridshell obtained by actuating the grid in (A). (C) Custom-fabricated hemispherical gridshells with $n = 5, 7, 9, 11$, $d_r = 0.254$ mm, and $R = 61.1$ mm, and (D) the corresponding actuated gridshells obtained by a series of DER simulations. Scale bars in (C) are 15 mm. (For interpretation of the references to colour in this figure legend, the reader is referred to the web version of this article.)

2. Definition of the problem

In this section, we define our problem on the study of the mechanical response of an elastic gridshell under indentation. Specifically, we detail the key components of the system, describe our procedure for the point-load indentation of these structures, and identify the research questions that we seek to address.

A gridshell originates from a *footprint* (Fig. 1A), a planar grid with a well-defined *initial boundary* (black dashed lines in Fig. 1A). The boundary of this footprint can be actuated to yield a three-dimensional shell-like structure. The footprint lies on the *xy*-plane, with two orthogonal sets of rods aligned with the *x*-axis and *y*-axis, respectively (see Fig. 1A for the definition of the axes). The two mutually orthogonal sets of rods are connected by *joints* at their crossing points. In our study, we limit our scope to joints with strong positional constraints but negligible torsional stiffness. As a result, each pair of cross-laid rods does not slide, but it can freely shear. We refer to *actuation* as the process whereby the originally flat footprint is made to buckle out-of-plane by displacing its extremities along an *actuation path* (red arrows in Fig. 1A). Pinned boundary conditions are enforced at the extremities of all the rods throughout the actuation process. The resulting structure (Fig. 1B) resembles a doubly-curved surface, even if, in reality, it is composed of multiple elastically deformed rods that are 'cross-linked' to one another by joints; hence, the *elastic gridshell* nomenclature.

In the previous study (Baek et al., 2018), we showed that the shape of boundary and the actuation path can be rationally designed using the theory of Chebyshev nets to yield the desired gridshell shape. The theory of Chebyshev nets was initially conceived as part of an effort to describe the kinematics of *textiles*–a medium which possesses anisotropic inextensibility (Tschebyscheff, 1878). We showed that the theory of Chebyshev nets can also be adopted for elastic gridshells. While a few research had been conducted to incorporate the theory of discrete Chebyshev nets framework into the computational design of mesh-like structures (Baverel et al., 2012; Garg et al., 2014; Hennicke et al., 1974; Hernández et al., 2013), our emphasis is on the connection between smooth Chebyshev nets and the rational design of gridshells. The hemispherical gridshell is a representative case for which we had managed to successfully harness the theory of Chebyshev nets for a predictive design. In fact, the initial boundary and the actuation path shown in Fig. 1A was obtained from the calculation

from Chebyshev himself, which we shall refer to as the *Chebyshev ansatz for the hemisphere* (Chebyshev, 1946; Ghys, 2011); in short, they managed to numerically solve the underlying Gauss equation for the hemispherical Chebyshev net to obtain the angle function, ω, which can be directly integrated to construct the initial boundary and the actuation path. We have shown that positional deviations of our hemispherical gridshells are less than 2% from the Chebyshev ansatz. In the current study, we shall exclusively focus on hemispherical gridshells obtained from these Chebyshev ansatzes. The rationale for this emphasis is twofold. First, we already have a rich knowledge on the actuated geometry of the hemispherical gridshell from the previous research and prefer to leave the other geometries realized in Baek et al. (2018) (saddles, cylinders and building block assemblies) for future studies. Secondly, the hemisphere is a canonical example of positive double-curved structures.

Hemispherical gridshells can be uniquely described by the following four parameters: the radius of the actuated hemispherical structure, R, the diameter of rods, d_r, Young's modulus of rods, E, and the number of rods per direction, n. The actual grid enclosed by the initial boundary (rendered image, Fig. 1A) comprises a square array of elastic rods that was obtained by equidistantly sampling the domain defined by the boundary itself so that the number of rods per direction is n. The resulting physical gridshell (Fig. 1B) is then obtained by pinning the extremities of the grid along the pre-determined actuation path predicted from the Chebyshev net calculation (Baek et al., 2018).

With this actuated hemispherical gridshell in hand, we will investigate its mechanical response to point-load indentation. The actuated gridshell is first clamped at its extremities and is then indented by a prescribed amount of indentation, δ_0, under imposed displacement conditions. Typical magnitude of indentation is kept small throughout the study ($\delta_0/R \sim 0.01$). Concurrently with the indentation, we measure the reaction force, F. Given the linear response (evidence for this linearity is provided in Section 4), the *rigidity* of the hemispherical gridshell is defined as the slope of the force-indentation curve, $K = F/\delta_0$ (units of force/length; [N/m]). As we have already discussed in Section 1, a plethora of past literature has been dedicated to rationalizing the rigidity of doubly-curved isotropic shells (Lazarus et al., 2012; Pogorelov, 1988; Reissner, 1946; Vella et al., 2012), to which we want to directly contrast our results. Our ultimate objective is to provide a reduced functional representation for K with respect to the four relevant parameters that define the geometry and the material properties of the structure: $K = \hat{K}(R, d_r, E, n)$. In short, we seek to quantify the linear response of hemispherical gridshells.

3. Physical and numerical experiments

To quantify the functional relationship for the geometric rigidity of the hemispherical gridshells, we follow an empirical approach that combines both desktop-scale physical experiments and numerical simulations. In the experiments, the set of parameters explored is: $R = \{38.2, 45.8, 53.5, 61.1, 68.8, 76.4\}$ mm; $d_r = \{0.203, 0.229, 0.254, 0.279\}$ mm; $E = 68.3$ GPa; and $n = \{1, 3, 5, 7, 9, 11, 13\}$. In parallel to the experiments, numerical simulations based on a discrete elastic rods (DER) method were conducted to more systematically and extensively explore the parameter space.

We will first detail the fabrication process of the nearly hemispherical gridshells. Secondly, we describe the numerical technique (the method of discrete elastic rods) which successfully mimics the physical fabrication process. Lastly, we describe the experimental and numerical procedures that we followed to apply the indentation and measure the following linear response of the elastic gridshells.

3.1. Fabrication of the hemispherical gridshell

Upon designing the flat (non-actuated) footprints that target a hemisphere upon actuation using the theoretical framework described in Section 2, we custom fabricated the hemispherical gridshells following our previously developed protocol (Baek et al., 2018). A brief overview of this fabrication procedure is provided next.

Given the theoretically computed footprint, we used a laser-cutter (LaserPro Spirit LS, Morgan Hill, CA) to etch a square network of grooves (the groove diameter, t_g, varies according to the diameter of the rods, d_r; $t_g = d_r$) onto two acrylic plates (thickness of the acrylic plates, $t_{mold} = 3.175$ mm). These two plates act as a die to keep the rods in place during fabrication. At each crossing points of any pair of perpendicular groove segments, cylindrical through-holes (diameter, $d_h = 3.0$ mm) were also laser-cut on the acrylic plates. These through-holes acted as molds for the flexible joints that eventually provide the positional constraints at the crossing points in the final grid (more below). We deliberately excluded the through-hole located at $x = y = 0$ in Fig. 1A, since it is the point where the point indentation will be applied (more on Section. 3.3). The exclusion of this joint at the pole of the gridshell is not problematic since, due to symmetry, the positional constraint at the pole plays a role in neither the actuation nor the indentation process. Nitinol rods (Confluent Medical Technologies, Fremont, CA) that are naturally straight were then press-fit onto the individual grooves of the acrylic plates, which were then apposed to form a single mold. The superelasticity of the Nitinol rods prevents the rods from plastic deformation during the actuation process, thus facilitating the fabrication. In our series of experiments, we fabricated a number of samples with Nitinol rods over the following range of diameters: $d_r = \{0.203, 0.229, 0.254, 0.279\}$ mm.

Once the mold containing the square grid of rods was assembled, Vinylpolysiloxane (Elite Double 8, Zhermack; Young's modulus $E_j = 0.23 \pm 0.01$ MPa) was then poured onto the cylindrical through-holes of the mold to cast cylindrical joints (joint diameter, $d_j = 3.0$ mm, joint height, $h_j = 6.35$ mm). Upon curing of the elastomeric joints, a speck of liquid glue (Loctite Professional Liquid Super Glue, Loctite, Düsseldorf, Germany) was applied at each joint to prevent sliding between the crossing rods, thereby enforcing positional constraints. The final step of the fabrication of the hemispherical elastic gridshells is the actuation of the 2D footprint into a 3D structure. To do so, we 3D-printed an annulus (White Strong and

Flexible, Shapeways, NY) onto which the extremities of the grid were clamped. In order to ensure the clamping conditions, this annulus was designed to contain a series of holes (clamping hole depth, $t_c = 6.0\,\text{mm}$, diameter, $t_c \leq$ 300 μm), whose positions and tangents had been pre-determined from the output of the Chebyshev net calculation. This rigid circular rim was also set as the equator of the final hemispherical grid and acted as the supporting base of the structure. The extremities of all rods were press-fit into the clamping holes, thereby imposing the desired clamped boundary conditions. Previously, we had considered the pinned boundary conditions during the investigation on the nonlocal deformation of the hemispherical gridshells (Baek et al., 2018); however, in this study, we do consider the clamped boundary conditions given its original application in the architecture, in which the clamp is valued for its structural performance. This choice also facilitates establishing a more direct comparison to the indentation of isotropic shells, for which pinned boundaries are rarely investigated.

In Fig. 1C, we present four representative examples of physical gridshells produced using the protocol described above, with $n = 5, 7, 9, 11$, $d_r = 0.254\,\text{mm}$, and $R = 61.1\,\text{mm}$. In Fig. 1D, we then report the results from the corresponding DER simulations, with identical geometric and material parameters to those of the experiments of Fig. 1C. Details of the DER simulations that are specific to the current investigation will be described in more detail in Section 3.2. We find that the experimentally fabricated gridshells are in excellent agreement with those predicted from the DER simulations, as we had already demonstrated in Baek et al. (2018), but now also for different numbers of rods, n, for each design.

3.2. DER simulations of the actuated geometry

In parallel to the experiments, we conducted a series of computer simulations to measure the rigidity of the hemispherical gridshells, identically to the experiments. This simulation algorithm is based on the discrete elastic rod (DER) method (Bergou et al., 2010; 2008; Jawed et al., 2018) that integrates the Kirchhoff's rod assumptions and modern developments in discrete differential geometry. DER has witnessed remarkable success in the computer graphics community for robust visualization of the geometrically nonlinear deformation of hair and fur. More recently, DER has shown to be powerful in accurately predicting the mechanics of filamentous structures found in numerous engineering mechanics (Jawed et al., 2014), with excellent quantitative agreement against experiments with no fitting parameters.

In Baek et al. (2018), we have also shown excellent quantitative agreement between the DER results and experiments in predicting the actuated shapes of hemispherical gridshells. The current investigation follows a computational protocol similar to that of our previous study. First, the grid geometry (Fig. 1A), together with the radius of the actuated hemisphere, R, and the number of rods, n, serve as the initial configuration of the simulation. The geometry is discretized with Kirchhoff rods (the number of segment per rods, $N_s = 250$, is fixed throughout the simulations) with the diameter d_r and Young's modulus E. The constraints between the two sets of cross-laid rods are modeled by stiff linear springs of stiffness $\kappa_s = 10^{-4}\,\text{N/m}$. Note that, the value of κ_s had been proven to be sufficiently large to ensure that the linear springs serve well as strong geometric constraints (Baek et al., 2018).

Actuation of the grid is done by prescribing quasi-static displacements to its extremities, connecting the boundary of the footprint and the circular equator of the targeted hemispherical gridshell. The choice of the actuation path was based on the previous observation that the actuation of the hemispherical gridshell is path-independent (Baek et al., 2018). During actuation, a jittering body force of intensity $g = 0.35\,N/\text{mm}^3$ (force per unit volume of the rods) was applied normal to the grid, serving as the imperfection that triggers the out-of-plane buckling. After the 3D actuated hemispherical structure was obtained, the gridshell was clamped along its boundary and held stationary to dampen out all the unsteady fluctuation due to inertia. This additional step is essential since DER is fully dynamic whereas our interest in on the quasi-static response.

As pointed out in Section 4.2, the actuated geometry of the computed hemispherical gridshells in Fig. 1D is in excellent agreement with the experimental counterpart of Fig. 1C. With this computed actuated structures in hand, the rigidity of the gridshells is investigated through the DER simulations. Details of the DER simulations specific to the indentation process, as well as the experimental procedure for the measurement of the rigidity, will be delineated next.

3.3. Indentation

We shall focus mainly on vertical indentation performed on the joint located at the upper pole of the gridshell. Indentation away from the pole will be considered in Section 7. Fig. 2A shows both the actuated, yet un-indented geometry (black solid lines), of a hemispherical gridshell ($n = 11$ and $R = 61.1\,\text{mm}$), as well as its indented geometry (red solid lines). Point indentation with a prescribed displacement, $\delta_o = 0.5\,\text{mm}$ (see inset of Fig. 2A), was applied at the apex of the gridshell under the imposed displacement conditions. The indentation was performed at a rate of $8.3\,\mu\text{m.s}^{-1}$, during which the reaction force, F, was measured. The indentation rate is slow enough for the process to be considered quasi-static. Note that, the indented configuration illustrated in Fig. 2A is magnified by a factor of 10× to ease visualization. Still, the deformation due to the indentation is small compared to the radius of the gridshell; the maximum value for the indentation-to-radius ratio throughout our investigation is $\delta_o/R = 0.013$. This small value of indentation ensures the linear response of the gridshells, as we shall demonstrate below (Fig. 3A and B).

In the experiments, the custom-fabricated gridshells were mounted onto the breadboard base of a universal testing machine (5943, Instron, Norwood, MA) and indented by a flat steel indenter of radius $R_i = 7\,\text{mm}$. Note that, within the range of parameters considered in this study, the value of R_i ensures that the indenter only touches the pole of the hemispherical gridshell, thereby guaranteeing the point indentation condition, mirroring what is also done in the simulations. Moreover,

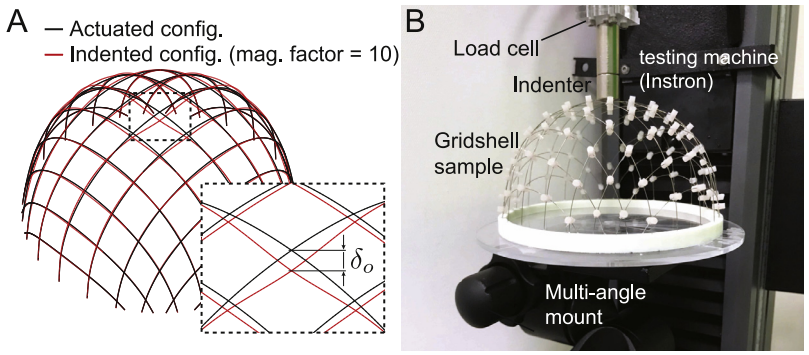

Fig. 2. (A) Schematic diagram of the indentation experiments. While each extremities being clamped, apex of the sample gridshell is indented by the prescribed amount, $\delta_o = 0.5\,\text{mm}$. Indentation of the other locations is also to be considered in Section 7. Black solid lines are the actuated configuration of the sample gridshell, and red solid lines are the indented configuration, with the magnification factor of 10. (B) Photograph of the experimental setup for indenting gridshells. Apex joint of the clamped hemispherical gridshell is indented, while the subsequent reaction force is measured by a universal testing machine (Instron). (For interpretation of the references to colour in this figure legend, the reader is referred to the web version of this article.)

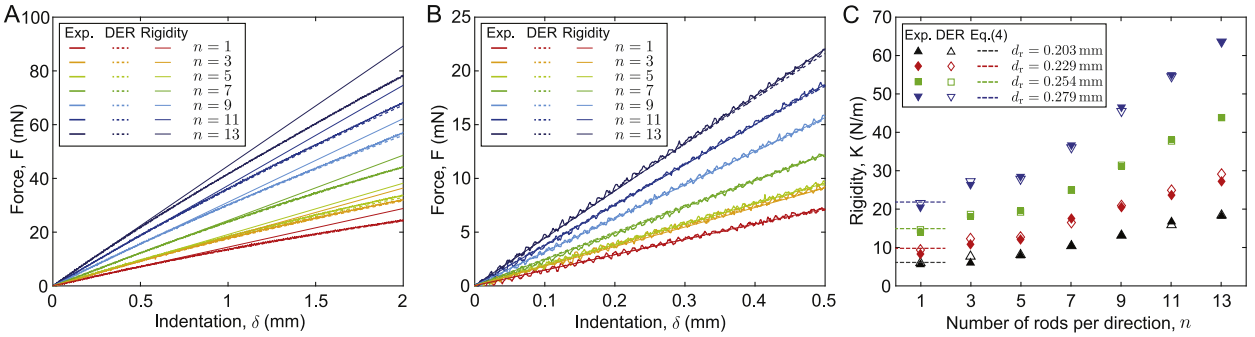

Fig. 3. (A) Load-displacement curves for the indentation at the apex of the gridshells, with $n = \{1, 3, \ldots, 13\}$, $R = 61.1\,\text{mm}$, and $d_r = 0.254\,\text{mm}$. The thick dashed and solid lines correspond to the DER simulations and experiments, respectively. The thin straight lines represent the corresponding rigidity measured in the linear regime, from the data in B. (B) Magnified view of (A) for the region $0 \le \delta \le \delta_o = 0.5\,\text{mm}$. (C) Rigidity of the gridshells, K[mN/mm], versus n, for four different values of the rod thickness, $d_r = \{0.203, 0.229, 0.254, 0.279\}\,\text{mm}$, obtained from the DER simulation (filled symbols), the experiments (open symbols), and the 2D-elastica theory (dashed lines; only when $n = 1$). Three independent indentation experiments were conducted for each configuration of the gridshells and their averaged values are plotted, with standard deviations that are smaller than the size of symbols.

since the joint at the pole is excluded during the fabrication process, the indentation reliably measures the rigidity of the gridshells, not that of gridshells combined with the stiffness of the joint. Just as in the DER simulations, an indentation of magnitude $\delta_o = 0.5\,\text{mm}$ is applied, and the corresponding reaction force, F, is measured by a load cell (2530-10 N Static Load Cell, Instron, Norwood, MA). The range of forces recorded in the full set of the experiments is $2.7 - 50.0\,\text{mN}$, ensuring that the finite resolution of the load cell (± 100 μ N) does not lead to any significant error in the measurements. For each configuration of the gridshells with different values of n and R, three independent experimental runs of indentation were conducted and averaged. We found that the standard deviation between these three runs was negligible (the corresponding error bars are smaller than typical symbol size of figures).

The setup described above enables for the rigidity of the gridshells to be measured at their pole. To quantify the rigidity away from the pole, we have enhanced the experimental apparatus by adding an adjustable geared head (410 Junior, Manfrotto, Cassola, Italy) that allows for the angle of the base of the gridshell to be varied, thereby imposing the indentation direction precisely. The direction of indentation is set to be along the normal vector on the gridshell, at an indentation point. The geometric information required to calculate this normal was obtained from the DER simulations. Unlike the experiments performed to measure the rigidity at the pole, we found that friction between the indenter and the gridshell affects the measured rigidity. Therefore, to minimize frictional effects, thereby preventing constraints of the in-plane displacement that is normal to the indentation direction, we applied silicone oil (WD-40 Specialist, WD-40 Company, San Diego, CA) at the indenter and the indentation points on the gridshell. Five independent indentation experiments were conducted and averaged, with standard deviation displayed as error-bars (see Fig. 6); still, the error bars in Fig. 6 are small, ensuring the robustness and consistency of our experimental protocol.

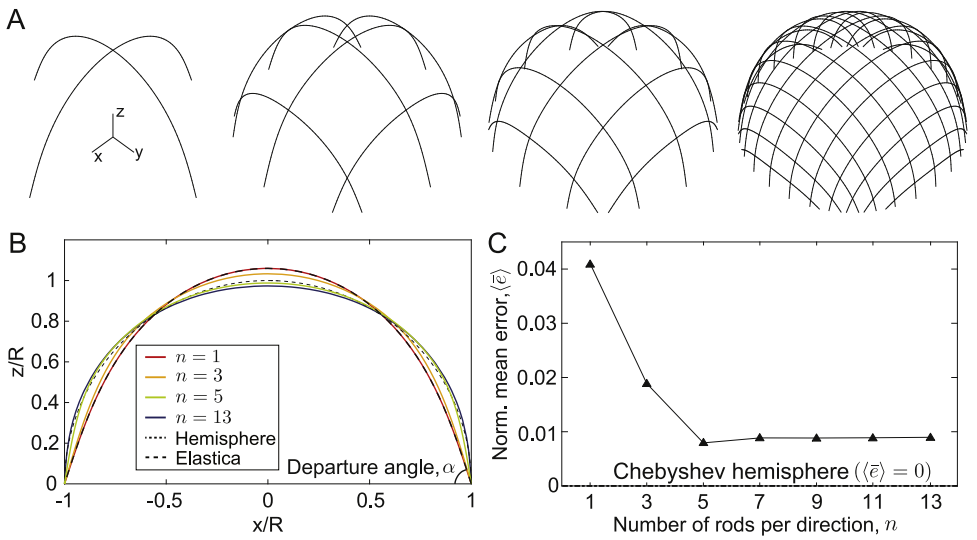

Fig. 4. Effect of the number of rods per direction, n, on the shape of the actuated hemispherical elastic gridshells, with $R = 61.1$ mm, and the diameter of rods, $d_r = 0.254$ mm. All the data are obtained from the DER simulations. (A) Shapes of actuated hemispherical elastic gridshells with varying $n = \{1, 3, 5, \ldots, 13\}$; the case $n = 1$ recovers two well-known Euler's elastica. (B) Shape of the central rods with respect to different values of n. Starting from $n = 5$, the solutions do not change much. (C) Plot of the average normalized mean error, $\langle \bar{e} \rangle$, versus n. $\langle \bar{e} \rangle = 0$ corresponds to the perfect Chebyshev hemisphere and $\langle \bar{e} \rangle = 0.041$ corresponds to the 2D elastica ($n = 1$). The error stabilizes after $n = 5$.

4. Indentation of elastic gridshells: rigidity versus density of rods

We start our investigation by focusing on the dependence of the rigidity of the elastic gridshell, K, on the number of rods per direction, n, of the footprint. In Fig. 3A, we plot a series of force-indentation curves, $F(\delta)$, for gridshells with different values of n, in the range of $1 \le n \le 13$. All other parameters are kept constant; in particular, $R = 61.1$ mm and $d_r = 0.254$ mm. The experimental results (solid curves) are juxtaposed with corresponding DER simulations (dashed curves) for the same parameter values, showing excellent quantitative agreement. This match between experiments and DER also conveys the validity and high-fidelity of the simulations that we will present for the remainder of this paper. In this first set of experiments, we chose the following range of indentation: $0 \le \delta \le 2$ mm. From the data in Fig. 3A, it is evident that the response becomes nonlinear toward the higher values of δ (*i.e.*, the experimental and simulation curves deviate from the thin/solid straight lines; more on these below).

Naturally, the rigidity needs to be measured in the linear regime of indentation. In Fig. 3B, we present a magnified view of Fig. 3A over the sub-region $0 \le \delta \le \delta_o = 0.5$ mm. In this range, the data in Fig. 3B exhibit a linear dependence of F on δ, whose slope is the rigidity of the gridshell, K, that we seek to rationalize. Therefore, our probing of the linear response of the gridshell is ensured by the chosen extent of indentation $\delta_o = 0.5$ mm, which is sufficiently small to preclude nonlinear effects effectively. As Fig. 3A illustrates, such nonlinearity is certainly present for higher values of $\delta > \delta_o$. However, even if interesting, we consider the nonlinear regime beyond the scope of the present investigation and leave it for a future study.

In Fig. 3C, we plot the values of K, obtained from the slope of the $F(\delta)$ curves, as a function of n. On that same plot we superpose data sets for different values of the rod diameter, $d_r = \{0.203, 0.229, 0.254, 0.279\}$ mm (a total of 28 different gridshell configurations). For each values of d_r, we find that K increases linearly with n, but only as long as $n \ge 5$. For $1 \le n < 5$, there is a deviation from this linear dependence of $K(n)$. In Section 4.1, we shall further investigate this off-trend by analyzing the actuated shapes of the corresponding gridshells. Moreover, we highlight that the case $n = 1$ corresponds to the classic Euler's elastica; the single joint located at the indentation does not provide any geometric constraints to the vertical indentation, due to the symmetry. In Fig. 3C, we also present the value for $K(n = 1)$ (horizontal dashed lines) predicted from the theory of elastica, whose details are discussed below in Section 4.2,

4.1. Dependence of the shape of the actuated gridshells on the number density of rods

Next, we turn to the off-trend behavior observed in Fig. 3C when $1 \le n < 5$, which, as we shall see, is related to the deviation of the corresponding shapes from the targeted perfect hemisphere. These deviations are because the footprint for the hemispherical gridshell is a *d-sampled* discrete sub-domain of the continuous Chebyshev domain. Therefore, the design framework for the theory of Chebyshev nets ceases to be valid when the number of rods in the grid is below a small threshold value ($n < 5$); in such cases, the number of rods is too small to enforce positional constraints between rods over the entire domain that would result in a nearly hemispherical actuated form.

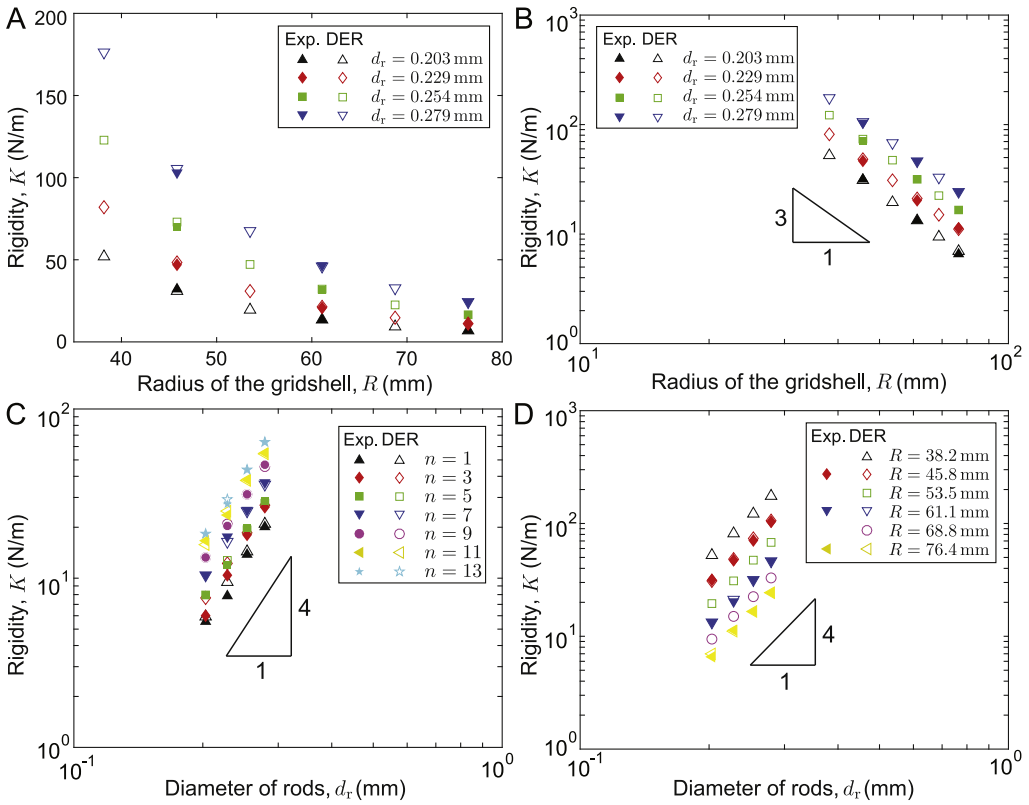

Fig. 5. (A) Effect of the radius of gridshells, R[mm], on the rigidity, K[N/m], for varying diameter of rods, $d_r = \{0.203, 0.229, 0.254, 0.279\}$ mm. DER simulations (empty symbols) are conducted for twenty-four different configurations while experiments are conducted for twelve different configurations. The number of rods per direction is kept $n = 9$. (B) Log-log plot clearly shows the cubic dependence of K on R. (C and D) Effect of the diameter of gridshells, d_r[mm], on the rigidity, K[N/m], for (C) varying number of rods of gridshells, $n = \{1, 3, 5, 7, 9, 11, 13\}$ and (D) varying radius of the gridshells, $R = \{38.2, 45.8, 53.5, 61.1, 68.8, 76.4\}$ mm. Each plots is obtained by rearranging Fig. 3C and Fig. 5A, respectively. From both cases, the power law $K \sim d_r^4$ is suggested.

In Fig. 4, we systematically assess these departures from the targeted hemisphere for elastic gridshells with $1 \leq n \leq 13$. First, we comment qualitatively on the overall shape of the actuated shapes. In Fig. 4A, we plot the centerline of the gridshells with $n = \{1, 3, 5, 13\}$, which we take as representative examples. When $n = 1$, the gridshell comprises two single rods, both of which lie on the surface of revolution that resembles an eggshell. These two rods have a single intersection at the pole of the structure, where they cross perpendicularly. This significant deviation from the hemisphere is because, due to symmetry, the positional constraint between the two rods in this particular elastic gridshell plays no role in determining the actuated shape; *i.e.* there is no geometric constraint. Below, in Section 4.2, we will show that this gridshell does lie on the surface of revolution generated by the shape of one of these Euler's elastica. When $n = 3$, even if a few additional constraints have been added to the gridshell, the resulting gridshell shape is still far from hemispherical.

As an alternative way to qualitatively comment on the shape of the gridshells for different values of n, in Fig. 4B, we plot the centerline of their central rod (one of the two rods passing the north pole; the other is identical by symmetry). We found that these shapes do not change dramatically when $n \geq 5$. Therefore, to avoid visual congestion in Fig. 4B, we only present the representative examples with $n = \{1, 3, 5, 13\}$. For the $n = 1$ and $n = 3$ cases, due to the reduced number of constraints imposed between the rods, the central rods exhibit an eggshell-like shape; the normalized height at their pole, $z/R(x = 0) = 1 + \epsilon$ (ϵ is an eccentricity, which measures deviation from a circular shape; a unit circle has $\epsilon = 0$), is larger than unity ($\epsilon = 0.06$ for $n = 1$ and $\epsilon = 0.03$ for $n = 3$). By contrast, for the $n = 5$ and $n = 13$ cases, ϵ is slightly lower than zero ($\epsilon = -0.01$ for $n = 5$ and $\epsilon = -0.03$ for $n = 13$). Moreover, the departure angle of the central rods, denoted as α in Fig. 4B, is 74^o for $n = 1$ and $n = 3$, whereas it is 81^o for $n = 5$ and 90^o for $n = 13$. The overall observation from Fig. 4B, along with the findings from Fig. 4A, is that our gridshells approximate the hemisphere only when $n \geq 5$, which is suggestive of a connection with the findings in Fig. 3C that the linear dependence of $K(n)$ on n is also only valid when $n \geq 5$.

In order to support the above qualitative evaluation, in Fig. 4C, we now quantify the deviation of the actuated shape of the gridshells from the hemisphere. To do so, we introduce a single-valued distance metric for the normalized mean error

of the obtained actuated gridshells from the targeted hemispherical configuration:

$$\langle \bar{e} \rangle = \frac{1}{N \cdot R} \sum_{i=1}^{N} e_i = \frac{1}{N \cdot R} \sum_{i=1}^{N} ||\mathbf{C}(\mathbf{x}_i) - \mathbf{G}(\mathbf{x}_i)||, \tag{1}$$

where N is the total number of nodes of the gridshell used in the simulation to discretize the grid geometry, $\mathbf{x}_i \in \mathbb{R}^2$ is the position of the i-th node in the un-actuated configuration, and $\mathbf{C}(\mathbf{x_{ii}})$ and $\mathbf{G}(\mathbf{x_{ii}})$ are the mapped positions of $\mathbf{x}_i$ in 3D which are from the Chebyshev hemisphere and the actuated gridshell, respectively. As an illustrative example, we expect $\langle \bar{e} \rangle = 0$ when the initially planar grid actuates exactly to the Chebyshev hemisphere of radius R. In short, this metric measures the extent to which, on average, the actuated gridshell deviates from its Chebyshev hemisphere, normalized by the radius of its base, R. Note that we previously employed this metric in Baek et al. (2018), where we showed that $\langle \bar{e} \rangle < 0.02$ for the experimental hemispherical gridshells designed from a Chebyshev construction.

In Fig. 4C, we plot $\langle \bar{e} \rangle$ for the gridshells with $1 \le n \le 13$. As expected, the $n \ge 5$ cases are nearly hemispherical ($\langle \bar{e} \rangle \le 0.01$). However, when $n = 1$ and $n = 3$, the value of $\langle \bar{e} \rangle$ is 0.041 and 0.019, respectively. Again, these deviations can be attributed to the fact that the number of rods is too small to enforce the sufficient positional constraints between two sets of rods over the entire domain, and this geometric deviation can be attributed to the off-trend behavior for the rigidity of the gridshells.

4.2. Indentation of a clamped elastica – the special case with $n = 1$

The actuated (yet un-indented) shape of gridshell with $n = 1$ is, in fact, the canonical problem of Euler's elastica. From the profiles in Fig. 4B, we found that the curve corresponding to the analytic solution for the Euler's elastica (dashed line; Euler and Carathéodory, 1952; Love, 2013; Saalschütz, 1880) is in excellent agreement with the shape of the central rod for a 'gridshell' with $n = 1$ (red solid line). Next, we seek to compute the rigidity of the hemispherical gridshell for this $n = 1$ case following a classic and well-established variational approach.

Consider a rod of length $2L = \pi R$ laid on an the x-axis, from $x = 0$ to $x = 2L$. The rod is described by the arc-length parametrization, s. During the actuation process, one of the extremities of this rod is compressed from $x = 2L$ to $x = 2R$ to induce buckling in the xz-plane. An indenting force, P, is then applied at the rod's midpoint, $s = L$, in the negative z-direction. It is important to note that the case with $P = 0$ (no indentation) is a textbook problem that has long been resolved by Euler (Euler and Carathéodory, 1952), even if a modern solution method based on hypergeometric functions has been proposed (Saalschütz, 1880). Still, for completeness, we believe that it is informative to revisit this calculation in detail, within the context of our present problem of indented elastic gridshells.

One half of the rod, $0 \le s \le L$, can fully be described by one kinematic variable, $\theta(s)$; the angle between the tangent at a point s and the x-axis. The positional coordinates of the curve, $(x(s), z(s))$, can then be expressed in terms of $\theta(s)$: $x(s) = \int_0^s \cos\theta(s)\mathrm{d}s$ and $z(s) = \int_0^s \sin\theta(s)\mathrm{d}s$, respectively. The underlying variables are then made dimensionless as: $\bar{\theta} \leftarrow \theta$, $0 \le \bar{s} \leftarrow s/L \le 1$, $\bar{x} \leftarrow x/L$, and $\bar{y} \leftarrow y/L$. The prime symbol ($'$) shall denote differentiation with respect to $\bar{s}$. Considering the first-order variations of the bending energy, work done by the force P, and the constraint imposed at $x = R$, one can then obtain the following system of ordinary differential equations (ODEs),

$$\bar{x}' = \cos\bar{\theta} \tag{2a}$$

$$\bar{z}' = \sin\bar{\theta} \tag{2b}$$

$$\bar{\theta}'' = \frac{PL^2}{B}\cos\bar{\theta} + \frac{\mu L^2}{B}\sin\bar{\theta}, \tag{2c}$$

where $B = EI = E\pi d_r^4/64$ is the bending stiffness of the rod. The corresponding boundary conditions are $\bar{x}(0) = 0$, $\bar{x}(1) = R/L = 2/\pi$, $\bar{z}(0) = 0$, $\bar{\theta}'(0) = 0$, and $\bar{\theta}(1) = 0$. Even if standard, the classical derivation of Eq. (2) is provided in Appendix A. The *Lagrange multiplier* μ (units of force) corresponds to the unknown force at $s = L$ along the x-direction that is required to maintain the shape of the elastica. Eq. (2) is then numerically solved using a shooting method (Stoer and Bulirsch, 2013). Setting $P = 0$ to find the actuated but yet un-indented configuration and the corresponding shooting variable, μ, we obtain the shape of the gridshell with $n = 1$, which will shall denote as $(\tilde{x}, \tilde{z}, \tilde{\theta}, \tilde{\mu};\ P = 0)$.

We proceed by considering the effect of an infinitesimal indenting force, $P = P_1$; the gridshell is clamped and Eq. (2) is perturbed with respect to the un-indented configuration. Setting $\bar{x} \to \tilde{x} + \bar{x}_1$, $\bar{z} \to \tilde{z} + \bar{z}_1$, $\bar{\theta} \to \tilde{\theta} + \bar{\theta}_1$, $\mu \to \tilde{\mu} + \mu_1$, and $P \to P_1$, we obtain the following system of ODEs for the incremental state variables:

$$\bar{x}_1' = -\bar{\theta}_1 \sin\tilde{\theta} \tag{3a}$$

$$\bar{z}_1' = \bar{\theta}_1 \cos\tilde{\theta} \tag{3b}$$

$$\bar{\theta}_1'' = \frac{P_1 L^2}{B}\cos\tilde{\theta} + \frac{\mu_1 L^2}{B}\sin\tilde{\theta} + \frac{\mu L^2}{B}\bar{\theta}_1\cos\tilde{\theta} \tag{3c}$$

with $\bar{x}_1(0) = 0$, $\bar{x}_1(1) = 0$, $\bar{z}_1(0) = 0$, $\bar{\theta}_1(0) = 0$, and $\bar{\theta}_1(1) = 0$ as boundary conditions. Similarly to above, Eq. (3) is solved numerically using a shooting method. In the process, the geometric rigidity can be obtained from the relationship between the amount of indentation, $\bar{z}_1(1)$, and the corresponding reaction force, P_1. We have computed the rigidity of the $n = 1$ gridshell to be:

$$K(n=1) = -4\frac{P_1}{\bar{z}_1(1)} = 11.98\frac{Ed_r^4}{R^3}. \tag{4}$$

The prefactor '4' in the above equation arises from the fact that Eq. (2) concerns only one half of the rod, while the gridshell with $n = 1$ is composed of four half-rods, and the negative sign in Eq. (4) is due to the fact that the direction of P_1 is along the negative-z axis. With this prediction for $K(n = 1)$ in hand, we now return to Fig. 3C, where we plotted K as a function of n, and now superpose Eq. (4) for different values of d_r (horizontal dashed lines). These predictions are in excellent agreement with both the experimental (filled symbols) and DER (open symbols) results.

Even if the above classic variational approach is successful in yielding $K(n = 1)$, it cannot be generalized for more complex gridshells with $n \geq 3$ due to the nontrivial positional constraints that arise at each joint. As such, introducing additional rods into the structure dramatically increases the complexity of the problem; Eq. (3) cannot account for the reaction forces between the multiple rods, and it is precisely these geometric constraints that enrich the mechanics of elastic gridshells.

5. Toward a dimensionless description for the rigidity of elastic gridshells

Taking an alternative point of departure from the variational approach of Section 4.2, now for $n \geq 3$, we proceed by turning to empirical scalings to describe the rigidity of our hemispherical gridshells. These scalings shall be proposed based on the data acquired from an extensive exploration of parameter space in physical and numerical experiments, with the relevant prefactors determined directly by fitting the data. This approach is chosen in lieu of directly tackling the full constrained Euler elastica theory, which would have been a challenging endeavor. Specifically, we focus on a nondimensional relation for $K = \hat{K}(R, d_r, E, n)$. We also seek to contrast the functional dependence of the expression for K of our elastic gridshells, against that of other common structural elements; *e.g.,* shells and beams. We then finish this section by proposing a master curve that successfully describes all the results from both the physical experiments and the DER simulations, across a wide range of parameters.

5.1. Dimensional analysis

The rigidity, K, has units of force per unit length, [N.m^{-1}]. Selecting E, d_r, n, and R as the primary set of relevant variables and applying the Pi theorem (Buckingham, 1914) yields an expression for the dimensionless rigidity that only depends on two nondimensional groups, n and d_r/R:

$$\bar{K} = \frac{K}{Ed_r} = f\left(n, \frac{d_r}{R}\right). \tag{5}$$

Interpreting d_r as a thickness-like quantity of the gridshells, we recognize Eq. (5) as an analog to Reissner's seminal result for the dimensionless rigidity of a continuum, isotropic hemispherical shell (Reissner, 1946),

$$\overline{K}_s = \frac{K_s}{Et} = \frac{4}{\sqrt{3(1-\nu^2)}}\left(\frac{t}{R}\right), \tag{6}$$

where K_s is the rigidity of the hemispherical shell of radius R and thickness t, made of an isotropic elastic material with Young's modulus, E, and Poisson's ratio, ν. For comparison, the geometric rigidity of a Euler elastica is (Euler and Carathéodory, 1952; Love, 2013)

$$K_e = c\frac{EI}{L^3}, \tag{7}$$

where EI is the bending modulus of the elastica, L is its total arc-length, and c is a dimensionless constant that depends on boundary conditions. For a circular elastic rod of diameter d, the bending modulus is $EI \sim Ed^4$. In this case, Eq. (7) can then be rewritten in dimensionless form as

$$\overline{K}_e = \frac{K_e}{Ed} = c\left(\frac{d}{L}\right)^3. \tag{8}$$

In Section 4, we presented data from both physical and numerical (DER) experiments on the dependence of K on n for gridshells. In what follows, we seek to further explore these data to specify the scaling relation for $\bar{K}$ according to Eq. (5) for our gridshells. For this purpose, in addition to the $K = \hat{K}(1 \leq n \leq 13)$ data that was already presented in Fig. 3C for gridshells with $R = 61.1$ mm and $d_r = 0.254$ mm, we need to more systematically investigate the dependence of K along other rays of the (R, d_r) parameter subspace.

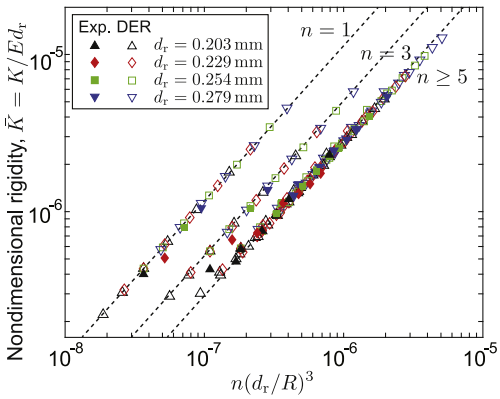

Fig. 6. A master curve, which gathers all the experiments (32 different configurations; filled symbols) and simulations (168 different configurations; empty symbols). Normalized rigidity, K/Ed_r, is plotted as a function of $n(d_r/R)^3$, leading to the scaling $K/Ed_r \sim n(d_r/R)^3$. The geometric deviation of the shape of gridshells from the shape of the perfect hemisphere results in the different prefactors for the cases $n = 1$, $n = 3$, and $n \geq 5$, leading to the offset in the log-log plot. Dashed lines are a fitting curve from each sets of simulations with $n = 1$, $n = 3$, and $n \geq 5$, respectively.

In Fig. 5A, we plot K as a function of R, at six different values of $R = \{38.2, 45.8, 53.5, 61.1, 68.8, 76.4\}$ mm and four different values of $d_r = \{0.203, 0.229, 0.254, 0.279\}$ mm obtained from DER simulations (open symbols); *i.e.*, a total of 24 gridshells. In this sweep of parameter space, the number of rods per direction was kept constant at $n = 9$. Given that the validity and accuracy of the DER simulations was already attested in Fig. 3, we decided to only conduct a subset of experiments ($R = \{45.8, 61.1, 76.4\}$ mm; a total of 12 physical gridshells (filled symbols in Fig. 5). Beyond these small set of experiments, which served as a double-check, we relied primarily on the DER simulations to explore the R dependence. Still, the excellent agreement found between experiments and DER continues to strengthen the validity of our methodology.

The log-log plot of Fig. 5B suggests that the dependence of the rigidity of our gridshells is consistent with the power-law $K \sim R^{-3}$. Note that this inverse cubic scaling is also found in the rigidity of the Euler's elastica in Eq. (8). This scaling is to be contrasted with the rigidity of continuum isotropic hemispherical shells, for which $K_s \sim R^{-1}$; see Eq. (6). This finding that $K \sim R^{-3}$ serves as the first piece of evidence that the force-scale of our elastic gridshells is set by elasticity (Euler's elastica) of the individual rod members, rather than shell-like quantities. Whereas this results may *a priori* appear as straightforward because the structures are comprised of a network of elastic rods, it is in fact far from trivial due to the strong geometric constraints imparted by the joints between the two sets of mutually orthogonal rods.

Even if it is evident from Eq. (5) that the results in Fig. 5A and B imply the power-law $K \sim d_r^4$, here we try to validate this more thoroughly by rearranging the existing data obtained from the physical and numerical experiments. In Fig. 5C and D, we revisit the data from Figs. 3 and 5 A and plot K as a function of d_r. The resulting log-log plots from the two independent set of experiments suggest the power-law $K \sim d_r^4$ under a wider range of parameters: $n = \{1, 3, 5, 7, 9, 11, 13\}$ and $R = \{38.2, 45.8, 53.5, 61.1, 68.8, 76.4\}$ mm. For a fixed value of n, Fig. 5B, together with Fig. 5D, suggest the power-law $K/Ed_r \sim (d_r/R)^3$. At first sight, the dynamic range of the data in Fig. 5B–D may appear limited for definitive claims of power-laws to be made but the recast of the data in dimensionless form presented in the next section will point further to the robustness of this scaling.

5.2. Master curve for the rigidity of hemispherical gridshells

In Fig. 6, we gather the entire set of experimental and numerical data presented thus far and plot the dimensionless rigidity, $\bar{K} = K/Ed_r$, as a function of $n(d_r/R)^3$. Beyond the 32 configurations of the hemispherical gridshells that were already presented in Figs. 3 and 5, additional simulations are also conducted for all the possible combinations of the parameters considered so far: $n = \{1, 3, 5, 7, 9, 11, 13\}$, $R = \{38.2, 45.8, 53.4, 61.1, 68.8, 76.3\}$ mm, and $d_r = \{0.203, 0.229, 0.254, 0.279\}$ mm; *i.e.*, a total of 168 different simulations. Remarkably, we find the data splits and then collapses into three clearly distinct master curves: (i) for $n = 1$, (ii) for $n = 3$ and (iii) for $n \geq 5$. We note that the extensive DER data (open symbols) continues to be in excellent agreement with the smaller set of experimental data (closed symbols), which were obtained for additional validation purposes.

All in all, our findings suggest that the rigidity of the elastic gridshells under point load indentation at their pole is well described by the following empirical relation:

$$\frac{K}{Ed_r} = b\,n\left(\frac{d_r}{R}\right)^3, \tag{9}$$

where b is a dimensionless prefactor that the above scaling analysis cannot provide and needs to be determined by fitting the data. For the three cases of the split master curves in Fig. 6, (i) $n = 1$, (ii) $n = 3$ and (iii) $n \geq 5$, the corresponding values of the prefactor in Eq. (9) are (i) $b(n = 1) = 11.66 \pm 0.02$, (ii) $b(n = 3) = 4.97 \pm 0.01$, and (iii) $b(n \geq 5) = 2.59 \pm 0.02$. It is remarkable that Eq. (9) successfully describes the full set of the acquired data (from experiments and simulations) given

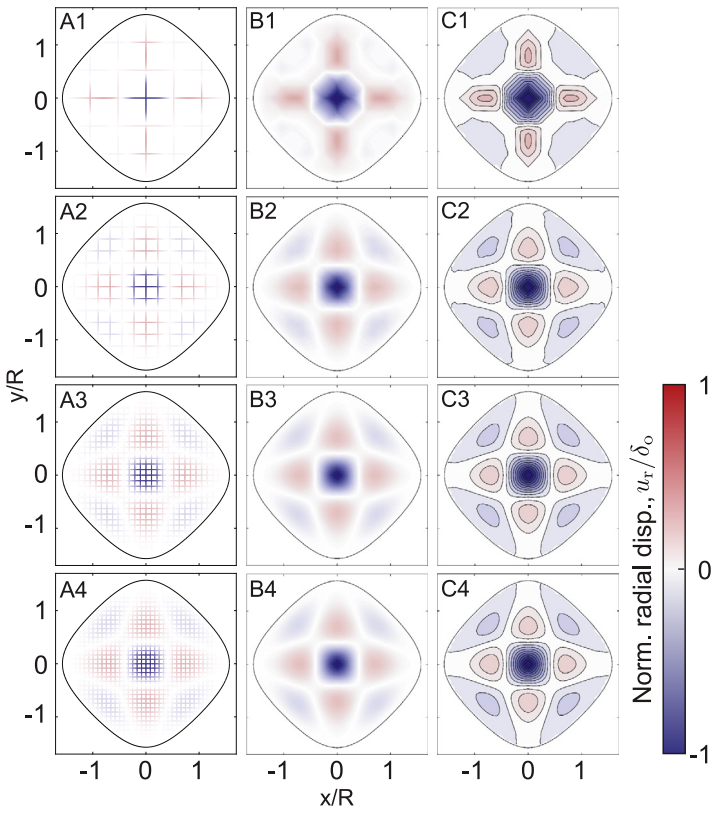

Fig. 7. (A) Displacement field, (B) interpolated displacement field, and (C) contours of the interpolated displacement field, for the gridshells with $n = \{5, 13, 29, 37\}$ (from the top row to the bottom row), $R = 61.1$ mm, and $d_r = 0.254$ mm, under the prescribed indentation, $\delta_o = 0.5$ mm. Colorbar represent the normalized radial displacement of the hemispherical gridshell, u_r/δ_o, where negative value means it is displaced towards the center of the hemispherical gridshell (thereby coinciding with a direction of the indentation). (For interpretation of the references to colour in this figure legend, the reader is referred to the web version of this article.)

the wide range of the parameters explored. In Fig. 4, we attributed the difference in behavior of the $n = 1$ and $n = 3$ cases, when compare to the more general $n \geq 5$, to their geometric deviations of the corresponding actuated gridshells from a hemispherical shape. It is, therefore, striking that the scaling relation in Eq. (9) holds for all values of n, while the geometric deviation appears to be directly related to the prefactor b.

From the perspective of continuum isotropic shells, the linear dependence of K on n is never trivial since K is a local quantity while n is not; unlike isotropic shells, rods far away from the indentation are all contributing to the local stiffness. Such linear dependence in Eq. (9) highlights the nonlocal nature of the rigidity of the gridshells, even if it is beyond the scope of the current study to fully rationalize b in terms of the relevant parameters of the hemispherical gridshell.

6. Interpolated deformation field under the point indentation

Having attributed the heterogeneous nature of the gridshell rigidity to a manifestation of nonlocality, we now place additional emphasis on the displacement field caused by indentation. Specifically, we interpolate the displacement field of the gridshell under the point of indentation and comment on the differences with continuum isotropic shells. We recall that, in our previous study (Baek et al., 2018), we had already provided some preliminary comments on the nonlocal behavior of gridshells. In this final section, now more systematically, we vary the number of rods (n) and quantify the resulting displacement field, which we shall show is independent of n that is sufficiently large. This asymptotic result points to the generality of our framework in grid structures containing a large number of rods.

In Fig. 7, we plot results obtained from simulations of gridshells with increasing number of rods $n = \{5, 13, 29, 37\}$, for the following quantities: (A) the radial displacement fields of the gridshell; (B) the interpolated radial displacement fields over the entire region spanned by the gridshell; and (C) the contour plot of the interpolated displacement field. We obtained the piecewise-linear interpolated displacement field from the displacement of each rods using a MATLAB command *fit*, using the actuated, un-indented configuration as the reference configuration in the calculations. However, for clarity, the computed displacement fields are shown on the grid configuration. Although it is not detailed in the results of Fig. 7, we have found that the interpolated fields do not depend on the other parameters of the gridshell such as E, R, and d_r. Hence, we chose to only represent the plots with varying n. The adjacent colorbar represents the radial displacement of the rods,

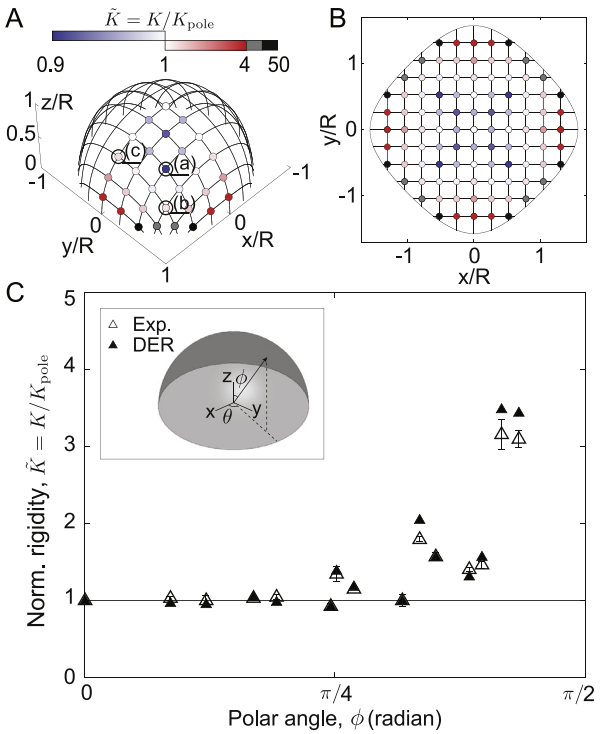

Fig. 8. Effect of the location of indentation on the gridshell rigidity. The prescribed indentation, normal to the surface spanned by the gridshell, is applied at every crossings of the hemispherical gridshell ($n = 11$, $R = 61.1$ mm). The adjacent colorbar represents the rigidity normalized by the value measured at the north pole, $\tilde{K} = K/K_{\text{pole}}$. The DER-predictions of $\tilde{K}$ are drawn (A) in the gridshell space and (B) in the grid space. The values of $\tilde{K}$ measured at the three chosen representative different locations are: (a) $\tilde{K}$ =0.92, (b) $\tilde{K}$ =1.38, and (c) $\tilde{K}$ =1.31. (C) The distribution of the dimensionless rigidity $\tilde{K}$, measured by experiments (open symbols) and DER simulations (solid symbols), is plotted as a function of the polar angle, ϕ. The dependence of $\tilde{K}$ on the azimuthal angle, θ, will be systematically investigated in Fig. 9.

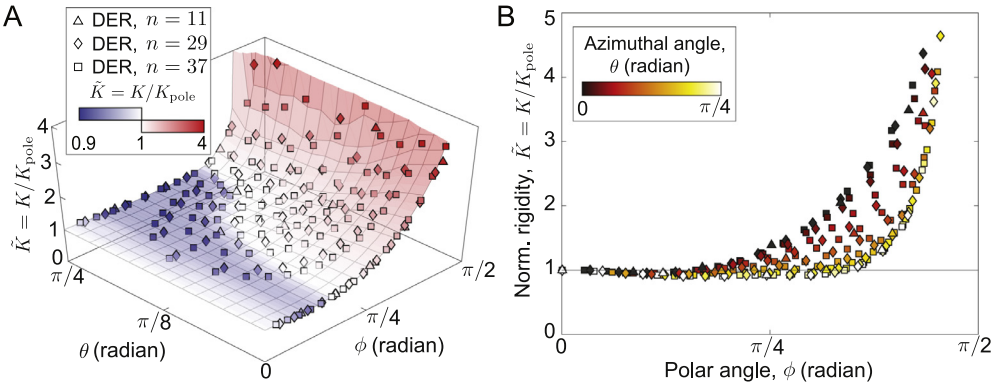

Fig. 9. Distribution of $\tilde{K} = K/K_{\text{pole}}$ as a function of the polar angle of the indentation location, ϕ, and the azimuthal angle, θ. Three different gridshells with $n = \{11, 29, 37\}$ and $R = 61.1$ mm are considered (see legend), and $K(\phi, \theta)$ is measured using the DER simulation. (A) 3-D plot of $\tilde{K}$ versus (ϕ, θ). (B) Projection of (A) onto the $\tilde{K} - \phi$ plane. The colorbar represents the azimuthal angle, θ.

normalized by the indentation magnitude, u_r/δ_o, where a negative value (blue) is indicative of a displacement towards the center of the hemisphere. It is important to note that the interpolated displacement fields presented in Fig. 7 appear to have an asymptotic state, even for gridshells that are as coarse as $n = 13$, thereby pointing to the generality of this results. These results suggests that a continuum description for this class of structures may be within reach, even if its development will require a theoretical effort that is beyond the scope of the current study.

The results shown in Fig. 7 reiterate the nonlocal response of our gridshell structures. This findings are in stark contrast to what we would have obtained for a isotropic shell, where the magnitude of the displacement field would have been zero everywhere except in the small vicinity of the locus of indentation (Nasto et al., 2013; Pogorelov, 1988; Vaziri and

Mahadevan, 2008). Again, we emphasize this nonlocality underlies the hitherto difficulty in rationalizing the mechanics of gridshells.

7. Probing the rigidity of the gridshells away from the pole

Finally, having rationalized the rigidity of our gridshell upon indentation at their pole, we now investigate indentation at other latitudes and longitudes. If it were for an isotropic hemispherical shell, the value of K would have been the same everywhere except near the clamped boundary since the rigidity of the continuum isotropic shell depends only on the local material properties (Young's modulus and Poisson's ratio) and curvature in the neighborhood of the indentation point (Lazarus et al., 2012; Vella et al., 2012). However, unlike isotropic shells, we found in Section 6 that elastic gridshells exhibit highly nonlocal deformation fields under point indentation. As a consequence of these nonlocal effects, we do not expect the rigidity of the gridshell to depend on the local geometry alone. In the final step of our study, we probe the gridshell away from its pole, while limiting the investigation to point loads only at the joints where the two initially orthogonal set of rods are cross-laid. Therefore, unlike an isotropic continuum shell, there exists a finite number of possible indentation locations.

In Fig. 6A, we present the spatial distribution of the gridshell's rigidity measured at the joints of the actual 3D actuated configuration, obtained exclusively from the DER simulations. Due to symmetry, only a quarter of the distribution is displayed. The adjacent colorbar represents the measured rigidity normalized by the rigidity at the pole, $\tilde{K} = K/K_{\text{pole}}$, with $K_{\text{pole}} = 38.2\,\text{N/m}$ for this particular gridshell ($R = 61.1\,\text{mm}$ and $n = 11$). In Fig. 6B, we also project the $\tilde{K}$ data from Fig. 6A into the originally flat (pre-actuation) 2D grid configuration. At the representative points (a), (b) and (c) labeled accordingly in Fig. 6A, the normalized rigidity is $\tilde{K} = 0.92,\ 1.38,$ and $1.31,$ respectively. Elsewhere in the hemisphere, the normalized rigidity varies in the range $0.92 \leq \tilde{K} \leq 45.41$. The maximal value of $\tilde{K} = 45.41$ (thus $K = 1.73\,\text{kN/m}$) occurs at the four points that are nearest to the equator of the structure, depicted as black filled circles in Fig. 6A and B. The second largest value of $\tilde{K} = 11.24$ is depicted as the gray filled circles. Excluding those eight extreme points near the equator, the value of $\tilde{K}$ falls into a range $0.92 \leq \tilde{K} \leq 3.48$. Overall, we find that rigidity of the gridshell possesses significant location sensitivity. In Fig. 6C, we characterize each indentation location on the gridshell as a polar angle, ϕ, measured from the apex of the hemisphere, and an azimuthal angle, θ, measured from the x-axis (see the inset of Fig. 6 for the definitions of the axes). As a validation of our simulation tool, we then plot our prediction for $\tilde{K}$, as a function of ϕ, on top of a series of experimental measurements. The results are again in excellent agreement with the experimental measurements which provides further support for our methodology.

With the goal of illustrating the nontrivial behavior of the rigidity of hemispherical gridshells in more detail, in Fig. 7, we further quantify the spatial dependence of $\tilde{K}$ by turning to a more extensive set of the DER simulations. Specifically, leveraging the accuracy of DER simulations demonstrated in Fig. 6C, we now also consider gridshells with the even larger number of rods per direction, $n = \{29,\ 37\}$, which then yield a larger number of different indentation locations. In Fig. 7A, we present $\tilde{K}$ as a function of ϕ and θ, for all three gridshells ($n = \{11,\ 29,\ 37\}$). Given the symmetry of the hemispherical gridshell, it is sufficient to consider the region $0 \leq \theta \leq \pi/4$. Toward aiding the visualization of the large set of data points distributed in the $(\phi,\ \theta,\ \tilde{K})$ space, we obtain piecewise-linear interpolated surface of the data from the $n = 29$ gridshell, using the MATLAB command *fit*. Interestingly, all the data from the other gridshells ($n = \{11, 39\}$), which did not participate in the fitting procedure, falls onto the interpolated surface. Again, this asymptotic behavior is a suggestive signature of the existence of suitable continuum description of the gridshell-like systems, as we have proposed in Section 6.

To help us better inspect the data, in Fig. 7B, we project Fig. 7A onto the $\phi - \tilde{K}$ plane, with the information on θ conveyed as a colorbar (inset). Overall, $\tilde{K}$ increases moderately until $\phi \simeq \pi/4$, after which there is a sharp increase as the equatorial clamped boundary is approached. Moreover, the azimuthal position of the indentation, θ, plays a prominent role over the entire range of ϕ. For any fixed values of ϕ, the points along $\theta = \pi/4$ are the most compliant. Furthermore, these simulations suggests a global minimum of $\tilde{K} = 0.902$ occurring at $(\phi,\ \theta) = (0.482,\ \pi/4)$ (units in radians). Note that, the value of $\tilde{K}$ below unity had also been observed in the physical gridshell with $n = 11$ (Fig. 6). On the other hand, the points along $\theta = 0$ are the most rigid spots of the gridshell.

Between the two extreme values of the polar angle, $\theta = 0$ and $\theta = \pi/4$, $\tilde{K}$ monotonically decreases as θ increases. In Fig. 7B, all the data points obtained from the gridshell with $n = \{11,\ 29,\ 37\}$ falls into the 'meniscus' formed by these two bounds of θ. We speculate that the $\theta = \pi/4$ curve is maximizing the shearing between rods while the $\theta = 0$ curve is maximizing the bending of the rods. Note that the gridshell responds to external loading by a combination of shearing and bending of the rods. However, since the shearing is un-constrained at the joints while the bending of the rods is important, the rigidity decreases as the shearing participates more in the deformation of the structure. This non-negligible heterogeneous response along θ further differentiates, qualitatively, the mechanical behavior of gridshells from that of the isotropic shells. Again, this scenario is a manifestation of the nontrivial anisotropic kinematics of gridshells. Although we have not yet been able to fully rationalize the rich mechanical behavior that underlies the location sensitivity of the rigidity, we hope that our results will instigate additional theoretical work along this direction.

8. Conclusion

We have quantified the rigidity, K, of hemispherical gridshells under point load indentation, following a primarily empirical approach using a combination of data from precision model experiments and computer simulations. First, we explored the rigidity at the pole of our structures. From this data, we obtained a robust scaling relation, Eq. (9), that is valid for the entire range of the design space that we explored. We investigated the following set of parameters: the radius of the hemisphere, R, the diameter of rods, d_r, the number of rods per direction, n, and the Young's modulus of the rods, E. At first glance, Eq. (9) may seem to indicate that it is indeed the elastica of the underlying rods that provides the rigidity of the entire structure. However, the linear dependence of K on n is far from trivial since it implies that all rods, even the rods away from the indentation point, contribute to the rigidity, as measured by a local point load indentation. We further inspected the nonlocality by quantifying the displacement field resulting from indentation at the pole. The fact that these displacement fields appear to converge to an asymptotic behavior for $n \geq 13$ calls for the development of a continuum description for this class of discrete structures. Moreover, we also investigated the rigidity away from the pole, finding that it increases nonlinearly as the equator of the gridshell is approached. The region of longitude $\theta = \pi/4$ always serves as a local soft region, while $\theta = 0$ as a local stiff region. The ensemble of our results points to the nonlocal nature of the mechanics of gridshells. This behavior is in contrast to continuum isotropic shells whose rigidity is local to the point of indentation.

Throughout our investigation, we implicitly focused on relatively *coarse* gridshells, whose distance between any pair of parallel rods is significantly larger than d_r ($n \times d_r/R \sim 0.01$, and, therefore, $n \sim 10$). Motivated by our finding of an asymptotic displacement field when $n > 13$, the study of *finer* gridshells (*i.e.*, with $n \times d_r/R \sim 1$ and $n \gg 100$) would be interesting for future research, calling for the development of a continuum framework for this structures. Fine gridshells could then be extended to general (beyond just hemispherical) two-dimensional structures with well-aligned filamentous sub-structures, as mundanely seen in knits, fabrics, and pasta strainers. Furthermore, beyond the idealized joints that we have considered in our model gridshells (fixed positional constraints and negligible torsional stiffness), future work on the fine gridshells may also need to address the interaction between adjacent rods, *e.g.*, frictional joints at the crossing point of two orthogonal rods/filaments.

In closing, we hope that the nontrivial, nonlinear and nonlocal behavior that we have uncovered in the mechanics of elastic gridshells will instigate future theoretical research in this rich class of structures.

Acknowledgments

This work was supported by the National Science Foundation, Faculty Early Career Development Program (CAREER) CMMI 1351449. We thank Basile Audoly and Corrado Maurini for useful discussions. We are particularly grateful to Andrew Sageman-Furnas, who gave our manuscript a careful read and with whom we have had extensive exchanges about elastic gridshells. Furthermore, he alerted us about an inconsistency that we had in the analysis of our data regarding the curvature of discrete structures, which we are able to address prior to submission of our manuscript; thank you. Finally, we express our sincere gratitude to an anonymous reviewer for helping us fix a crucial issue in DER simulations. The problem was identified when we addressed the Reviewer's request to add a layer of experimental validation to the results in Section 7. We also thank Khalid Jawed for an advice on how to implement this fix in the numerics.

Appendix A. Derivation of Eq. (2)

Assuming the inextensible and twist-free rods, the total elastic energy of (the half of) the rod is only from the bending due to the actuation, and is written as

$$E_b = \frac{1}{2}\int_0^L B\left(\frac{\mathrm{d}\theta}{\mathrm{d}s}\right)^2 \mathrm{d}s. \tag{A.1}$$

Moreover, the work done by the prescribed force, P, at $s = L$ is

$$W = -\int_{\delta_o}^{\Delta} P\,\mathrm{d}\Delta \tag{A.2}$$

where $\Delta = z(s = L)$ is the z-displacement due to P. The minus sign in Eq. (A.2) is due to the fact that the direction of P is negative-z. Lastly, the symmetric kinematic constraint requires

$$C = -R + x(L) = 0. \tag{A.3}$$

Taking the first-order variations of Eqs. (A.1)–(A.3) with respect to θ and applying the principle of virtual work (Audoly and Pomeau, 2010), we obtain the integral relation for any kinematically admissible first-order variation, $\delta\theta$, as,

$$\delta E_b - \delta W - \mu\delta C = \int_0^L \left[-B\frac{\mathrm{d}^2\theta}{\mathrm{d}s^2} + P\cos\theta + \mu\sin\theta \right]\delta\theta\,\mathrm{d}s = 0. \tag{A.4}$$

Localization of Eq. (A.4), with proper nondimensionalization of variables presented in Section 4.2, yields Eq. (2).

Supplementary material

Supplementary material associated with this article can be found, in the online version, at 10.1016/j.jmps.2018.11.002.

References

Audoly, B., Pomeau, Y., 2010. Elasticity and Geometry: From Hair Curls to the Non-Linear Response of Shells. Oxford University Press.

Baek, C., Sageman-Furnas, A.O., Jawed, M.K., Reis, P.M., 2018. Form finding in elastic gridshells. Proc. Natl. Acad. Sci. 115 (1), 75–80.

Baverel, O., Caron, J.-F., Tayeb, F., Peloux, L.D., 2012. Gridshells in composite materials: construction of a 300 m2 forum for the solidays' festival in paris. Struct. Eng. Int. 22 (3), 408–414. doi:10.2749/101686612X13363869853572.

Bergou, M., Audoly, B., Vouga, E., Wardetzky, M., Grinspun, E., 2010. Discrete viscous threads. ACM Trans. Graphics 29 (4), 116.

Bergou, M., Wardetzky, M., Robinson, S., Audoly, B., Grinspun, E., 2008. Discrete elastic rods. ACM Trans. Graphics 27 (3), 63.

Buckingham, E., 1914. On physically similar systems; illustrations of the use of dimensional equations. Phys. Rev. 4 (4), 345.

Bulenda, T., Knippers, J., 2001. Stability of grid shells. Comput. Struct. 79 (12), 1161–1174.

Castle, T., Cho, Y., Gong, X., Jung, E., Sussman, D.M., Yang, S., Kamien, R.D., 2014. Making the cut: Lattice kirigami rules. Phys. Rev. Lett. 113, 245502. doi:10.1103/PhysRevLett.113.245502.

Chebyshev, P.L., 1946. On the cutting of garments. Uspekhi Mat Nauk 1 (2(12)), 38–42.

Dudte, L.H., Vouga, E., Tachi, T., Mahadevan, L., 2016. Programming curvature using origami tessellations. Nat. Mater.

Erb, R.M., Sander, J.S., Grisch, R., Studart, A.R., 2013. Self-shaping composites with programmable bioinspired microstructures. Nat. Commun. 4, 1712.

Euler, L., Carathéodory, C., 1952. Methodus inveniendi lineas curvas maximi minimive proprietate gaudentes sive solutio problematis isoperimetrici latissimo sensu accepti. Birkhäuser.

Fu, H., Nan, K., Bai, W., Huang, W., Bai, K., Lu, L., Zhou, C., Liu, Y., Liu, F., Wang, J., et al., 2018. Morphable 3d mesostructures and microelectronic devices by multistable buckling mechanics. Nat. Mater. 17 (3), 268.

Garg, A., Sageman-Furnas, A.O., Deng, B., Yue, Y., Grinspun, E., Pauly, M., Wardetzky, M., 2014. Wire mesh design. ACM Trans. Graphics 33 (4), 1–12.

Ghys, É., 2011. Sur la coupe des vêtements: variation autour d'un thème de Tchebychev. Enseign Math. 57 (1–2), 165–208.

Gladman, A.S., Matsumoto, E.A., Nuzzo, R.G., Mahadevan, L., Lewis, J.A., 2016. Biomimetic 4d printing. Nat. Mater.

Hennicke, J., Matsushita, K., Otto, F., Sataka, K., Schaur, E., Shirayanagi, T., Gröbner, G., 1974. Grid Shells (IL 10). Inst Lightweight Structures, Stuttgart.

Hernández, E.L., Sechelmann, S., Rörig, T., Gengnagel, C., 2013. Topology optimisation of regular and irregular elastic gridshells by means of a non-linear variational method. In: Advances in Architectural Geometry 2012. Springer Vienna, Vienna, pp. 147–160.

Jawed, M.K., Da, F., Joo, J., Grinspun, E., Reis, P.M., 2014. Coiling of elastic rods on rigid substrates. Proc. Natl. Acad. Sci. USA 111 (41), 14663–14668.

Jawed, M.K., Novelia, A., O'Reilly, O.M., 2018. A Primer on the Kinematics of Discrete Elastic Rods. Springer.

Lazarus, A., Florijn, H., Reis, P.M., 2012. Geometry-induced rigidity in nonspherical pressurized elastic shells. Phys. Rev. Lett. 109 (14), 144301.

Lefevre, B., Douthe, C., Baverel, O., 2015. Buckling of elastic gridshells. J. IASS 56, 153–171.

Liddell, I., 2015. Frei otto and the development of gridshells. Case Stud. Struct. Eng. 4, 39–49.

Love, A.E.H., 2013. A Treatise on the Mathematical Theory of Elasticity. Cambridge university press.

Miura, K., 1985. Method of packaging and deployment of large membranes in space. The Institute of Space and Astronautical Science report.

Nasto, A., Ajdari, A., Lazarus, A., Vaziri, A., Reis, P.M., 2013. Localization of deformation in thin shells under indentation. Soft Matter 9 (29), 6796–6803.

Nasto, A., Reis, P.M., 2014. Localized structures in indented shells: a numerical investigation. J. Appl. Mech. 81 (12), 121008.

Overvelde, J.T., Weaver, J.C., Hoberman, C., Bertoldi, K., 2017. Rational design of reconfigurable prismatic architected materials. Nature 541 (7637), 347.

Pipkin, A.C., 1984. Equilibrium of Tchebychev nets. Arch. Ration Mech. An 85 (1), 81–97.

Pogorelov, A.V., 1988. Bendings of Surfaces and Stability of Shells, 72. American Mathematical Society.

Poincloux, S., Adda-Bedia, M., Lechenault, F., 2018. Geometry and elasticity of a knitted fabric. Phys. Rev. X 8, 021075. doi:10.1103/PhysRevX.8.021075.

Quinn, G., Gengnagel, C., 2014. A review of elastic grid shells, their erection methods and the potential use of pneumatic formwork. Mob. Rapidly Assem. Struct. IV.

van Rees, W.M., Vouga, E., Mahadevan, L., 2017. Growth patterns for shape-shifting elastic bilayers. Proc. Natl. Acad. Sci. 114 (44), 11597–11602.

Reis, P., Jaeger, H., van Hecke, M., 2015. Designer matter: a perspective. Extreme Mech. Lett. 5, 25–29.

Reis, P.M., 2015. A perspective on the revival of structural (in)stability with novel opportunities for function: from buckliphobia to buckliphilia. J. Appl. Mech. 82 (11), 111001.

Reissner, E., 1946. The flexural theory of shallow spherical shells. J. Math. Phys 25 (1), 80–85.

Rivlin, R.S., 1955. Plane strain of a net formed by inextensible cords. Indiana U Math. J. 4, 951–974.

Saalschütz, L., 1880. Der belastete Stab unter Einwirkung einer seitlichen Kraft: Auf Grundlage des strengen Ausdrucks für den Krümmungsradius.... Teubner.

Savin, T., Kurpios, N.A., Shyer, A.E., Florescu, P., Liang, H., Mahadevan, L., Tabin, C.J., 2011. On the growth and form of the gut. Nature 476 (7358), 57.

Shyu, T.C., Damasceno, P.F., Dodd, P.M., Lamoureux, A., Xu, L., Shlian, M., Shtein, M., Glotzer, S.C., Kotov, N.A., 2015. A kirigami approach to engineering elasticity in nanocomposites through patterned defects. Nat. Mater. 14 (8), 785.

Steigmann, D.J., 2018. Continuum theory for elastic sheets formed by inextensible crossed elasticae. Int. J. Non Linear Mech.

Stoer, J., Bulirsch, R., 2013. Introduction to Numerical Analysis, 12. Springer Science & Business Media.

Tachi, T., 2013. Designing freeform origami tessellations by generalizing resch's patterns. J. Mech. Des. 135 (11), 111006.

Tschebyscheff, P.L., 1878. Sur la coupe des vêtements, On the cutting of garments. Assoc franç pour l'avancement des sci 154–155.

Van West, B., Pipes, R., Keefe, M., 1990. A simulation of the draping of bidirectional fabrics over arbitrary surfaces. J. Text. Inst. 81 (4), 448–460.

Vaziri, A., Mahadevan, L., 2008. Localized and extended deformations of elastic shells. Proc. Natl. Acad. Sci. USA 105 (23), 7913–7918.

Vella, D., Ajdari, A., Vaziri, A., Boudaoud, A., 2012. Indentation of ellipsoidal and cylindrical elastic shells. Phys. Rev. Lett. 109 (14), 144302.

Wang, W.-B., Pipkin, A.C., 1986. Inextensible networks with bending stiffness. Q. J. Mech. Appl. Math. 39 (3), 343.

Wang, W.B., Pipkin, A.C., 1987. Plane deformations of nets with bending stiffness. Acta Mech. 65 (1–4), 263–279.

Xu, S., Yan, Z., Jang, K.-I., Huang, W., Fu, H., Kim, J., Wei, Z., Flavin, M., McCracken, J., Wang, R., et al., 2015. Assembly of micro/nanomaterials into complex, three-dimensional architectures by compressive buckling. Science 347 (6218), 154–159.

Zhang, Y., Yan, Z., Nan, K., Xiao, D., Liu, Y., Luan, H., Fu, H., Wang, X., Yang, Q., Wang, J., et al., 2015. A mechanically driven form of kirigami as a route to 3d mesostructures in micro/nanomembranes. Proc. Natl. Acad. Sci. 112 (38), 11757–11764.